J. Fluid Mech. (2000), *vol.* 412, *pp.* 279–301. Printed in the United Kingdom

© 2000 Cambridge University Press

Normal stresses and microstructure in bounded sheared suspensions via Stokesian Dynamics simulations

By ANUGRAH SINGH AND PRABHU R. NOTT

Department of Chemical Engineering, Indian Institute of Science, Bangalore 560 012, India
e-mail: prnott@chemeng.iisc.ernet.in

(Received 7 June 1999 and in revised form 21 January 2000)

We report the normal stresses in a non-Brownian suspension in plane Couette flow determined from Stokesian Dynamics simulations. The presence of normal stresses that are linear in the shear rate in a viscometric flow indicates a non-Newtonian character of the suspension, which is otherwise Newtonian. While in itself of interest, this phenomenon is also important because it is believed that normal stresses determine the migration of particles in flows with inhomogeneous shear fields. We simulate plane Couette flow by placing a layer of clear fluid adjacent to one wall in the master cell, which is then replicated periodically. From a combination of the traceless hydrodynamic stresslet on the suspended particles, the stresslet due to (non-hydrodynamic) inter-particle forces, and the total normal force on the walls, we determine the hydrodynamic and inter-particle force contributions to the isotropic 'particle pressure' and the first normal stress difference. We determine the stresses for a range of the particle concentration and the Couette gap. The particle pressure and the first normal stress difference exhibit a monotonic increase with the mean particle volume fraction $\bar{\phi}$. The ratio of normal to shear stresses on the walls also increases with $\bar{\phi}$, substantiating the result of Nott & Brady (1994) that this condition is required for stability to concentration fluctuations. We also study the microstructure by extracting the pair distribution function from our simulations; our results are in agreement with previous studies showing anisotropy in the pair distribution, which is the cause of normal stresses.

1. Introduction

It is often assumed in studies devoted to the creeping flow of suspensions of non-Brownian particles in Newtonian liquids that the rheological behaviour of the mixture is Newtonian, with an enhanced shear viscosity; considerable effort has been focused on the determination of the effective viscosity of suspensions as a function of the particle concentration and size distribution. However, some recent studies have reported the presence of normal stresses in viscometric flows that vary linearly with the shear rate (Prasad & Kytomaa 1995; Brady & Morris 1997). The existence of rate-dependent normal stresses is a non-Newtonian characteristic because the pressure in a Newtonian fluid in a viscometric flow is determined solely from the boundary conditions and the hydrostatic balance of forces; there is no rate dependence of the pressure. The presence of suspended particles causes an additional pressure that is linear in the shear rate. There is also evidence of normal stress differences in suspensions, which is clearly a non-Newtonian effect.

https://doi.org/10.1017/S0022112000008375 Published online by Cambridge University Press

The normal stresses in a non-colloidal suspension are worthy of investigation from a fundamental standpoint as they are the only non-Newtonian characteristics it exhibits – shear thinning or thickening or any viscoelastic effects are generally not observed unless there are significant non-hydrodynamic interactions between the suspended particles. From a practical viewpoint, normal stress differences are an important consideration in the processing of concentrated suspensions. Such a study is of even greater significance because normal stresses determine segregation of particles in suspensions subjected to an inhomogeneous shear field (Jenkins & McTigue 1990; Nott & Brady 1994). While the normal stresses show no apparent effect in a homogeneous suspension undergoing uniform deformation, Nott & Brady (1994) argued that their role in inhomogeneous shear is important; in the case of pressure-driven flow through a channel, for instance, they determine segregation through the requirement that normal stress in the gradient direction remain constant. Nott & Brady also showed that their 'suspension balance' model reduces to the 'diffusive flux' model of Leighton & Acrivos (1987) as a special case, showing that the two descriptions, though motivated by different considerations, were physically equivalent.

In the early investigations which attempted to calculate the bulk stress in a suspension (Batchelor 1970; Brady & Bossis 1985), the particle pressure (the isotropic component of the particle-induced stress) was discounted as being of no consequence. Phung, Brady & Bossis (1996) determined the normal stress differences in Brownian suspensions for a range of the Péclet number Pe, from simulations of unbounded plane shear; their data showed the first and second normal stress differences to be negative and comparable in magnitude at large Pe. Recently, Brady & Morris (1997) presented an analysis for dilute suspensions showing that an interplay between hydrodynamics, weak Brownian motion and a repulsive inter-particle force results in an anisotropic pair-distribution function; there is a buildup of particles of $O(Pe)$ in the compression quadrant, in a boundary layer of thickness $O(Pe^{-1})$. Since their solution for the pair distribution was valid only in the compression quadrant, they were unable to compute the complete hydrodynamic stress (except in the case of a very long-range repulsive force), but estimated part of the hydrodynamic contribution to the second normal stress difference in planar extensional flow.

The earliest reported measurement of the normal stress in suspensions was by Bagnold (1954). Though he attempted to investigate rheology in the 'macro-viscous' regime, the Reynolds number for his system was not sufficiently small, and most of his data were for the 'grain-inertia' regime, where stress is generated primarily by particle collisions. Gadala-Maria (1979) appears to have made more careful measurements of the normal stress in the creeping flow regime, but only for very concentrated suspensions. The most recent and systematic experiments were by Prasad & Kytomaa (1995) on concentrated suspensions ($0.493 < \phi < 0.561$), conducted with the stated aim of studying the "behaviour of the normal stress in the viscous regime, if it exists". However there appear to be several aspects in their study that strongly suggest the presence of artifacts: first, it does not appear that the density of the particles and suspending fluid were closely matched, leaving open the possibility of inhomogeneities arising from sedimentation. Secondly, their figures 8 and 9 show that the normal and shear stresses are roughly linear in the shear rate only for the smallest particle concentration ($\phi = 0.493$) and sub-linear at higher concentrations. This suggests stress generation by particle contacts, perhaps as a result of gravitational compaction. Lastly, they use a perforated top plate "that allows pore pressure to equilibrate" with unsheared pure fluid, so that the measured stress "results solely from the coupling

https://doi.org/10.1017/S0022112000008375 Published online by Cambridge University Press

of the particulate medium and the wall". This is an unconvincing argument because the stress in the viscous regime is transmitted solely by the fluid, and not by particle contacts – it thus appears that the stress that Prasad & Kytomaa measured was not the viscous stress but that arising from particle contacts.

Recently, Haan & Steif (1993) have determined the 'particle-phase pressure' from numerical simulations of a planar suspension of rough contacting cylinders subjected to shear. They incorporate the roughness as a minimum distance of separation, δ, between approaching cylinders. However, they define the dispersive pressure as the difference between the pressures in the particle and fluid phases, which is different from the usual definition of the particle-induced stress. A more detailed discussion of their study is given in the concluding section of this paper.

The model of Jenkins & McTigue (1990) and Nott & Brady (1994) provides a clear link between rheology and particle migration; it predicts migration of particles from regions of high to low shear rates in rectilinear flows if the normal stress in the gradient direction is an increasing function of particle concentration. The recent work of Morris & Boulay (1999) follows the speculation of Nott & Brady that normal stress *differences* modulate migration in curvilinear flows; they have shown that their model predictions are in qualitative agreement with data reported in the literature for shear in parallel-plate and cone–plate devices, if the ratio of the normal stresses is within a specified range.

In this paper, we report normal stresses determined from Stokesian Dynamics simulations. In the past, the stress from simulations has been determined by considering unbounded shear generated by the use of Lees–Edwards periodic boundary conditions, as in the work of Brady & Bossis (1985) and Phung *et al.* (1996). We do not follow this approach; rather we determine the stress for shear between plane parallel walls, i.e. plane Couette flow, just as one would in an experiment. We briefly describe the simulation method in § 2, in particular the extension of the original Stokesian Dynamics technique (Brady & Bossis 1988; Brady *et al.* 1988) to incorporate plane boundaries. In § 3 we report the shear and normal stresses determined from our simulations for a range of volume fraction of particles, and the pair-distribution function for some representative cases. A brief discussion and concluding remarks follow in § 4.

2. Simulation method

We focus on the dynamics of a non-Brownian suspension of spheres in a Newtonian liquid in the creeping flow regime, i.e. $Re_p \equiv \rho\dot{\gamma}a^2/\eta \to 0$ and $Pe \equiv \dot{\gamma}a^2/2D \to \infty$. The former is the Reynolds number based on particle size and the latter is the Péclet number; here ρ and η are the density and viscosity of the fluid, a is the radius of the spheres, $\dot{\gamma}$ is a nominal shear rate and D is the Brownian diffusivity of an isolated particle. Additionally we restrict our attention to neutrally buoyant suspensions (the densities of the spheres and suspending fluid are equal), though this constraint is not essential for the simulations and can easily be relaxed.

The Stokesian Dynamics method (Brady & Bossis 1988; Brady *et al.* 1988; Durlofsky & Brady 1989) has been used extensively for simulating the dynamics of a suspension of rigid spheres in a Newtonian fluid. In one of the early implementations of this technique, Durlofsky & Brady (1989) studied the shear of a suspension bounded between two plane parallel plates. They computed interactions between particles and the walls by discretizing the latter into patches and assuming a uniform distribution of the force density in each patch. They accounted for interactions between a particle

https://doi.org/10.1017/S0022112000008375 Published online by Cambridge University Press

in the master cell and another outside it by a mean-field approximation. This was later rectified by Brady *et al.* (1988) by the use of Ewald's resummation technique for a periodic lattice in order to simulate unbounded flow, which Nott & Brady (1994) subsequently used to study the pressure-driven flow of a suspension. Nott & Brady considered the walls to be made up of spheres stuck together by the requirement that they moved with the same velocity. Though the use of this 'bumpy' wall did not alter the large-scale dynamics of the suspension, it understandably resulted in particles near the walls recording a bumpy motion, which they subtracted off while computing the mean velocity fluctuation.

To avoid this and other complications arising from a bumpy wall and at the same time to simulate plane Couette flow that is unbounded in the flow and vorticity directions, we undertook to extend the Stokesian Dynamics method to allow plane boundaries. This was accomplished in a rather simple manner, the details of which are presented below.

The hydrodynamic forces and stresslets on the particles are related to their velocities and the imposed deformation rate by the relation

$$\begin{bmatrix} \boldsymbol{F} \\ \boldsymbol{S} \end{bmatrix} = \mathscr{R} \cdot \begin{bmatrix} \boldsymbol{U} - \langle \boldsymbol{u} \rangle \\ -\langle \boldsymbol{e} \rangle \end{bmatrix}. \tag{2.1}$$

The essence of the Stokesian Dynamics method is in decomposing the grand resistance tensor into far-field and near-field components:

$$\mathscr{R} = \mathscr{M}^{-1} + \mathscr{R}_{2b} - \mathscr{R}_{2b}^{\infty}, \tag{2.2}$$

where $\mathscr{M}$ is the far-field mobility tensor determined from a multipole expansion of the force density distribution on the particles, $\mathscr{R}_{2b}$ is the near-field two-body resistance tensor for all particle pairs and $\mathscr{R}_{2b}^{\infty}$ is the far-field part of $\mathscr{R}_{2b}$, which is subtracted to avoid double-counting. The near-field resistance contribution is added only when particle pairs are within a critical distance of each other, which was taken as a centre-to-centre distance of four radii in the studies cited above. While $\mathscr{M}$ is computed at the two-body level, its inverse captures all the many-body interactions, as shown by Durlofsky, Brady & Bossis (1987).

Our only modification of the above scheme is to use the exact sphere–wall resistances for interactions of the suspended particles with either of the bounding walls. For separations (distance of particle centre from the wall) between 1.01 and 3 radii, these were tabulated at discrete intervals of the separation and utilized in the code by interpolation. For separations less than 1.01 radii, the analytical form of the lubrication resistances was used (Brenner 1961; Maude 1961; Goldman, Cox & Brenner 1967). The far-field sphere–wall mobility is still computed as before, as a multipole expansion of the force density; in other words, the walls are discretized as a string of spheres (of the same size as the suspended spheres) to compute the far-field interactions. While this differs from the approach of Durlofsky & Brady (1989) of discretizing the walls into patches (with the force density assumed constant on each patch), its efficacy in computing the grand mobility is not inferior – the details of the force distribution on each discretized part of the wall will not significantly influence the motion of a particle far away from a wall. On the other hand, this ansatz enables us to use the efficient method of Brady *et al.* (1988) for computing $\mathscr{M}$ as a lattice sum using Ewald's resummation technique, in the simulation of uniformly sized spheres employing periodic boundary conditions.

Thus, the sphere–wall resistance $\mathscr{R}_{\boldsymbol{FU}}^{sw}$ for each wall is computed by summing the mobility inverse over all the discretizations (which are thought of as spheres for the

https://doi.org/10.1017/S0022112000008375 Published online by Cambridge University Press

purpose of calculating $\mathscr{M}$) in that wall, then adding the exact near-field sphere–wall resistance and lastly subtracting the far-field part of the resistance. In other words,

$$\mathscr{R}^{sw}_{FU} = \sum_k (\mathscr{M}^{-1})^{sk}_{FU} + \boldsymbol{R}^{sw}_{FU} - \boldsymbol{R}^{sw\,\infty}_{FU}, \tag{2.3}$$

where the summation above is over all the mobility discretizations in the wall.

The far-field part of the sphere–wall resistance, $\boldsymbol{R}^{sw\,\infty}_{FU}$, is determined by forming a mobility matrix for a sphere and all the wall 'particles', and then inverting. Computation of the near-field resistance tensor $\boldsymbol{R}^{sw}_{FU}$ is described below.

2.1. *Near-field sphere–wall hydrodynamic interactions*

For the general motion of a single sphere near a plane wall whose normal is in the y-direction, the force and torque (in the absence of shear) are related to the translational and rotational velocities as

$$\begin{bmatrix} F_x \\ F_y \\ T_z \end{bmatrix} = \begin{bmatrix} R_{F_xU_x} & 0 & R_{F_x\Omega_z} \\ 0 & R_{F_yU_y} & 0 \\ R_{T_zU_x} & 0 & R_{T_z\Omega_z} \end{bmatrix} \begin{bmatrix} U_x \\ U_y \\ \omega_z \end{bmatrix}. \tag{2.4}$$

When the separation ΔY between a sphere and a plane wall is less than 1.001, asymptotic expressions given by Goldman *et al.* (1967) for $R_{F_xU_x}$, $R_{F_x\Omega_z}$ and $R_{T_z\Omega_z}$, and by Cox & Brenner (1967) for $R_{F_yU_y}$ are used; for $1.001 < \Delta y < 3$, the bispherical harmonics solution of O'Neill (1964) for $R_{F_xU_x}$ and $R_{F_x\Omega_z}$, and the corrected solution of Dean & O'Neill (1963) for $R_{T_zU_x}$ and $R_{T_z\Omega_z}$, are used to compute the respective resistances and tabulate their values. Lastly, the series expansion of Brenner (1961) and Maude (1961) is used for generating the tabular data for $R_{F_yU_y}$.

2.2. *Simulation of plane Couette flow*

In order to simulate bounded plane shear, the suspension is restrained between two plane parallel walls translating relative to each other at a constant speed U_0. This cell cannot, however, be replicated periodically in the y-(gradient) direction, and therefore we have introduced a layer of pure fluid below the lower wall, as shown in figure 1. When this cell, comprising the layer of suspension restrained between the two walls and the layer of pure fluid, is replicated periodically in all directions, a negative shear rate is imposed on the suspension and a positive shear rate on the layer of pure fluid. The distance between the two walls containing the suspension is henceforth referred to as the Couette gap. In all our simulations, the Couette gap H is equal to the thickness of the layer of pure fluid, and the length L of the master cell is equal to H. The master cell is replicated periodically in all directions to generate fully developed flow between plane parallel walls.

The velocities of the walls are fixed and the forces on them are to be determined, while the forces on the particles are fixed and their velocities are to be determined. The velocities of the suspended particles are to be determined from

$$\mathscr{R}^{ss}_{FU}\cdot(\boldsymbol{U}^s - \langle\boldsymbol{u}\rangle) + \mathscr{R}^{sw}_{FU}\cdot(\boldsymbol{U}^w - \langle\boldsymbol{u}\rangle) = \boldsymbol{F}^s \tag{2.5}$$

where the superscripts s and w on the velocities and forces indicate sphere and wall quantities, and the superscripts ss and sw on the resistances indicate sphere–sphere and sphere–wall couplings, respectively. Similarly the forces on the walls are given by

$$\mathscr{R}^{ws}_{FU}\cdot(\boldsymbol{U}^s - \langle\boldsymbol{u}\rangle) + \mathscr{R}^{ww}_{FU}\cdot(\boldsymbol{U}^w - \langle\boldsymbol{u}\rangle) = \boldsymbol{F}^w. \tag{2.6}$$

https://doi.org/10.1017/S0022112000008375 Published online by Cambridge University Press

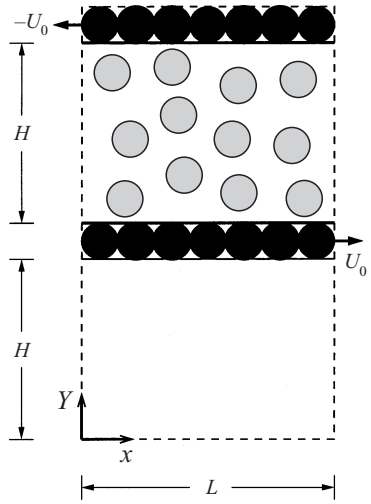


FIGURE 1. The master cell for our simulations of shear of a monolayer of spheres between plane parallel walls. For the purpose of computing the far-field sphere–wall interactions, it is assumed that each wall is composed of a plane of spheres. Note the layer of pure fluid, which allows periodic replication of this cell in the y-direction. The thickness of the layer of suspension H is henceforth referred to as the Couette gap.

In order to ensure that the flow in the Couette gap is uniform shear and there is no pressure-driven flow, the mean velocity over the entire domain, $\langle \boldsymbol{u} \rangle$, is set to zero. In some of our simulations we employed the alternative constraint

$$\sum_{\text{walls}} F_x = 0, \tag{2.7}$$

where the summation is over both walls, which again is an attempt to impose the condition that the flow is pure shear. While neither of the conditions above result in the mean velocity within the gap being exactly zero, we have verified in all our simulations that it is indeed very small (see § 3). Both conditions yielded almost identical bulk properties, so we shall only report results of simulations for which the former condition was used.

Equations (2.5) and (2.6) give the hydrodynamic forces on the spheres and walls. The dynamics of the spheres and walls is determined, once the external force is specified, by

$$\boldsymbol{F}_{\text{hyd}} + \boldsymbol{F}_{\text{ext}} = 0. \tag{2.8}$$

While we have imposed no external body force in our simulations, we have imposed an inter-particle repulsive interaction between the spheres. Besides providing a qualitative model of non-hydrodynamic effects when the inter-particle separation is small, the repulsive interaction also prevents frequent particles overlaps. Recently Dratler & Schowalter (1996) have shown that Stokesian Dynamics simulations employing a short-range repulsive force result in more realistic microstructure. The form of the repulsive force we have used is the same as in the simulations of Nott & Brady (1994),

$$\boldsymbol{F}_{\alpha\beta} = F_0 \frac{\tau \mathrm{e}^{-\tau\epsilon}}{1 - \mathrm{e}^{-\tau\epsilon}} \boldsymbol{e}_{\alpha\beta}, \tag{2.9}$$

where $\boldsymbol{F}_{\alpha\beta}$ is the force exerted by sphere β on sphere α. The parameters τ and F_0 specify the range of the force and its magnitude, respectively; ϵ is the separation

https://doi.org/10.1017/S0022112000008375 Published online by Cambridge University Press

between the surfaces of the spheres and $\boldsymbol{e}_{\alpha\beta}$ is the unit vector connecting the sphere centres. We have not imposed any non-hydrodynamic forces between the suspended particles and the walls.

The hydrodynamic stresslets on the particles are readily computed, once their velocities are known, from the relation

$$\mathscr{R}^{ss}_{\boldsymbol{SU}}\cdot(\boldsymbol{U}^s - \langle\boldsymbol{u}\rangle) + \mathscr{R}^{sw}_{\boldsymbol{SU}}\cdot(\boldsymbol{U}^w - \langle\boldsymbol{u}\rangle) = \boldsymbol{S}. \tag{2.10}$$

Substituting for $\boldsymbol{U}^s$ from (2.5), we get

$$\boldsymbol{S} = \mathscr{R}^{ss}_{\boldsymbol{SU}}\cdot(\mathscr{R}^{ss}_{\boldsymbol{FU}})^{-1}\cdot\boldsymbol{F}^s - \mathscr{R}^{ss}_{\boldsymbol{SU}}\cdot(\mathscr{R}^{ss}_{\boldsymbol{FU}})^{-1}\cdot\mathscr{R}^{sw}_{\boldsymbol{FU}}\cdot(\boldsymbol{U}^w - \langle\boldsymbol{u}\rangle) + \mathscr{R}^{sw}_{\boldsymbol{SU}}\cdot(\boldsymbol{U}^w - \langle\boldsymbol{u}\rangle). \tag{2.11}$$

We identify the first term on the right-hand side of the above relation as a contribution to the stresslet from the repulsive inter-particle forces and the remainder as a purely hydrodynamic stresslet. While this division is not strictly correct, as the inter-particle forces also determine the microstructure and hence the resistance functions $\mathscr{R}_{\boldsymbol{SU}}$ and $\mathscr{R}_{\boldsymbol{FU}}$, it serves as a convenient and useful measure of the respective contributions. However, we must emphasize that all contributions in (2.11) arise from *hydrodynamic interactions*, i.e. due to the relative motion of particles in the suspending fluid. There is a contribution to the stress from inter-particle forces which exists even in the absence of any intervening fluid, which (2.11) does not include; this contribution is accounted for while computing the net stress due to the inter-particle force in (3.4).

An important point to note here is that the far-field mobility $\mathscr{M}$ is constructed with the assumption that the hydrodynamic stresslet does not have an isotropic part, and hence the isotropic part of $\boldsymbol{S}$ determined from (2.11) is not complete. As detailed in § 3.1, we determine the full isotropic pressure by measuring the normal force on the walls.

Equation (2.5) is solved for the sphere velocities by Cholesky factorization, as $R^{ss}_{\boldsymbol{FU}}$ is symmetric and positive definite (Durlofsky *et al.* 1987). The hydrodynamic force exerted by the fluid on the wall is then given by (2.6), which must be balanced by an external force to keep it translating at constant velocity. From the forces on the walls, the shear and normal stresses in the suspension are readily determined. Our results in the following section are presented in dimensionless units: all lengths are scaled by the particle radius a, velocities by the wall speed U_0, time by a/U_0, and stresses by the product of the fluid viscosity η times the nominal shear rate $2U_0/H$.

All computations were performed on DEC Turbolaser 8400 workstations (140.4 MFLOPS). A simulation with 46 particles for a dimensionless time span of 5000 required 8 hours of CPU time.

3. Results

To verify our simulation technique, particularly the method of incorporating plane boundaries, we compare the translation velocity of a single sphere in plane Couette flow with the exact solution of Ganatos, Weinbaum & Pfeffer (1982). For the purpose of this comparison, we conducted a full three-dimensional simulation (i.e. the suspended sphere was allowed all six translational and rotational degrees of freedom), with the walls in the master cell measuring 14 sphere radii in the x- and z-directions, and separated by a distance of 10 sphere radii in the y-direction. Thus, each wall consists of 49 spheres for the mobility discretization. The top wall moves with a constant speed U_0 in the negative x-direction and the bottom wall with same speed

https://doi.org/10.1017/S0022112000008375 Published online by Cambridge University Press

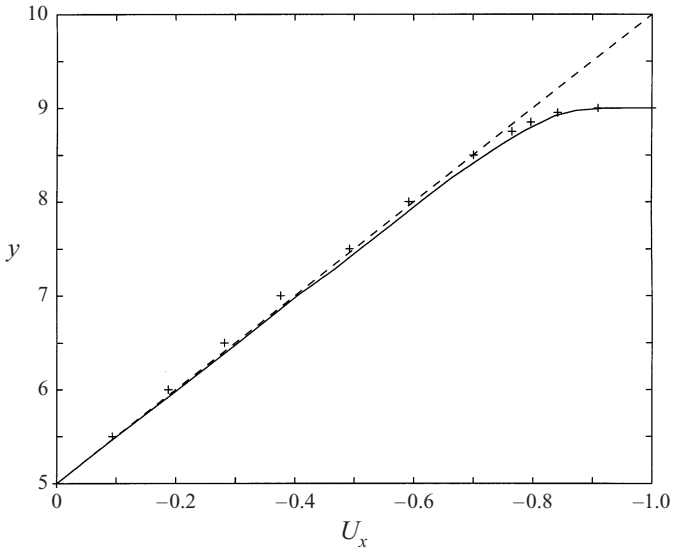


FIGURE 2. The translational velocity, as a function of position, of a single force- and torque-free sphere suspended in a fluid which is sheared between two planes spaced 10 sphere radii apart. The symbols are the results of our simulation, the solid line is the result of Ganatos *et al.* (1982), and the dashed line is the linear velocity profile for pure fluid.

in the opposite direction. The velocity of a single suspended sphere, which is force- and torque-free, is then determined as a function of its distance from the walls.

Figure 2 shows the translational velocity of the sphere (normalized by U_0) at different positions. Our result shows good agreement with the solution of Ganatos *et al.* (1982) near the walls, but deviates from it away from the walls. The discrepancy is, however, never greater than 6%. The deviation arises mainly from the approximation in Stokesian Dynamics of the hydrodynamic interactions as a matched sum of the near- and far-field contributions. There may also be a contribution to the error from the small pressure-driven component of the flow (see below). In any case, we expect the present scheme to suffice in capturing all the macroscopic properties of interest, as in the earlier studies that have employed this simulation technique.

All the results reported henceforth are for sheared suspensions of spheres confined to a monolayer. The centres of all suspended spheres in the master cell lie in the (x, y)-plane, and are restricted from translating in the z-direction. Additionally, rotational movement of the spheres is allowed in the z-direction only. The z-dimension of the master cell is 2 (i.e. 1 particle diameter), and it is replicated periodically in all directions. Simulations of a monolayer require far less computation, as not only are the spheres fewer in number, but the degrees of freedom for each sphere are also reduced to 6 (from 11 for a full three-dimensional simulation). However, the essential physics of the problem is retained in a monolayer simulation, as is evident from earlier studies (Brady & Bossis 1985; Nott & Brady 1994; Phung *et al.* 1996).

The parameters that determine the properties of the system are the mean area fraction of particles $\bar{\phi}$, the dimensionless Couette gap H, the strength of the repulsive force F_0, and its range τ. The initial configuration of the suspended spheres was generated by first arranging the particles in a regular array and then applying small random displacements until a uniform distribution was achieved. The steady-state response of all bulk properties was found to be largely insensitive to the initial

https://doi.org/10.1017/S0022112000008375 Published online by Cambridge University Press

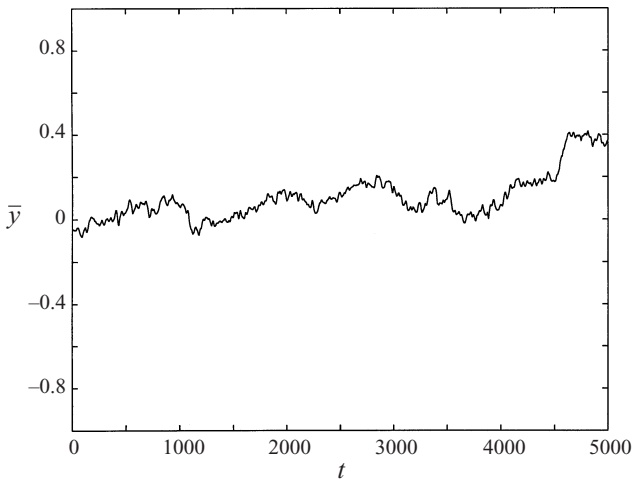


FIGURE 3. Trace of the mean distance of particles from the mid-plane ($y = 15$) versus time with the mean area fraction of spheres $\bar{\phi}$ set to 0.4 and the Couette gap H set to 30. The parameters for the repulsive inter-particle interaction (see equation (2.9)) are $F_0 = 10^{-4}$ and $\tau = 100$.

configuration as the microstructure quickly relaxed to its dynamical equilibrium. In all the simulations the structure was allowed to evolve from start till $t = 3000$, and the properties such as the concentration, velocity and stress fields were then averaged over the subsequent 2000 dimensionless time units. We ensured that the properties being measured were indeed those of a dynamical steady state by verifying that their average over a short time interval did not vary appreciably with time. It must be noted, however, that there are large intermittent fluctuations in the stress, especially at the higher particle concentrations that we have studied, corresponding to instances of the formation of a large (sometimes gap-spanning) network of particles. We have performed simulations for $H = 14$, 18 and 30, and for several values of $\bar{\phi}$ in the range 0.05 to 0.65.

Figure 3 shows the time trace of the mean distance of the particles from the mid-plane (scaled by the particle radius) for a mean area fraction of 0.40 and a Couette gap of 30. This simulation was carried out for a dimensionless time span of 5000, with a time increment of 0.01. As expected, there is no large-scale migration of the particles. The small increase in $\bar{y}$ towards the end of the simulation is due to a single sphere getting 'attached' to the top wall; we have verified that these instances have no effect on the bulk properties such as the stress. The particle concentration field, shown in figure 4, is uniform but for the expected depletion near the walls. Profiles of the particle concentration, velocity and other fields are obtained in the usual manner by dividing the simulation cell into a number of rectangular bins, determining the area-weighted mean in every bin at each instant, and then time averaging. The velocity profile for this simulation (also shown in figure 4) is linear across the gap. The mean velocity over all particles in the gap is never greater than 0.01, substantiating our assertion in § 2.2 that the pressure-driven component of the flow is very small. Another quantity of interest in the dynamics of suspensions is the mean-square fluctuation velocity of the suspended particles. Other than its obvious connection to the particle diffusivity, this field was also linked to the particle pressure in the suspension and migration of particles in inhomogeneous flows by Nott & Brady (1994). It is surprising that the mean-square fluctuation velocity (figure 5) shows a marked variation across

https://doi.org/10.1017/S0022112000008375 Published online by Cambridge University Press

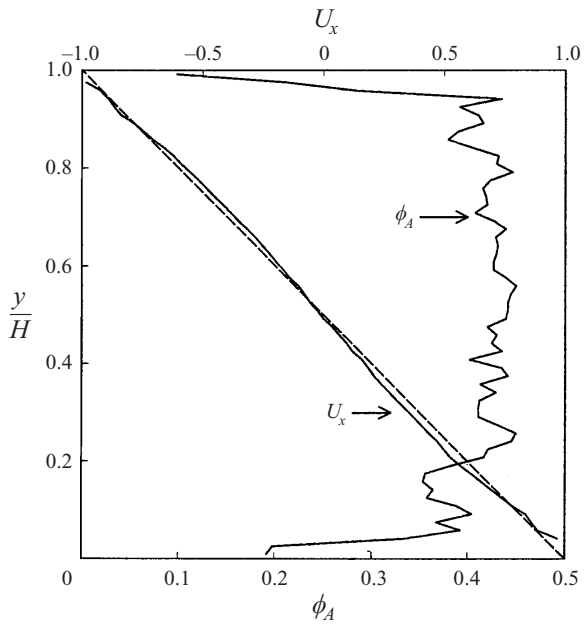


FIGURE 4. The steady-state concentration and velocity profiles for $\bar{\phi} = 0.4$ and $H = 30$. The dashed line is the linear velocity profile for a pure fluid. The parameters for the repulsive inter-particle force are as in figure 3.

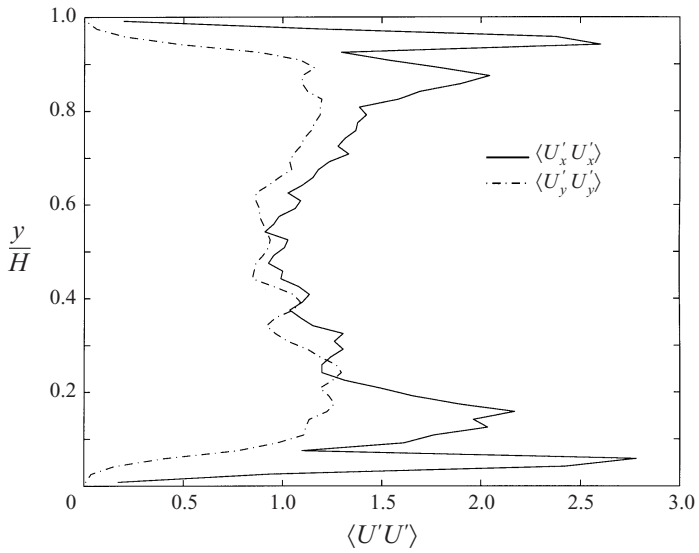


FIGURE 5. The time-averaged steady-state mean-square fluctuation velocity profile for $\bar{\phi} = 0.4$ and $H = 30$. Here U' has been scaled with $U_0(a/H)$, i.e. the product of the nominal shear rate and particle radius. The parameters for the repulsive inter-particle force are as in figure 3.

the gap though the shear rate is uniform, indicating its sensitivity to proximity to the impermeable walls.

The trends shown in figures 3–5 are indeed common to all our simulations. The mean velocity profile is always close to linear, the particle concentration is uniform

https://doi.org/10.1017/S0022112000008375 Published online by Cambridge University Press

across the Couette gap, and the fluctuation velocity rises with increasing proximity to the walls.

3.1. *Shear and normal stresses*

The shear stress σ_{yx} can be determined either by computing the net force on the walls in the x-direction, or from the mean stresslets on the suspended particles. While the normal stress differences can be determined from the stresslet S_{xx} and S_{yy}, the isotropic part of the stress, the particle pressure, cannot be determined correctly from the stresslet. As stated in § 2.2, this is because the mobility matrix $\mathscr{M}$, which accounts for the far-field part of the hydrodynamic interactions, was constructed assuming that $\sum_i S_{ii} = 0$ (the near-field interactions are accounted for by the exact two-body resistance, $\mathscr{R}_{2b}$, and therefore do capture the isotropic part of the stresslet). Jeffrey, Morris & Brady (1993), have computed the resistance functions that determine the full isotropic part of the stresslet, and these may be used to compute the particle pressure. However, we choose the more direct method of determining the pressure from the normal force on the walls, as shown below.

The net normal stress σ_{yy} may be written as

$$\sigma_{yy} = -\Pi^H_{ff} + \frac{N}{V}\left\{\langle S^H_{yy}\rangle + \langle S^P_{yy}\rangle\right\}, \tag{3.1}$$

where Π^H_{ff} is the far-field part of the stresslet, which was ignored while computing $\mathscr{M}$ (see above). The mean hydrodynamic particle stresslet $\langle \boldsymbol{S}^H\rangle$ is given by

$$(1-\phi)\langle \boldsymbol{S}^H\rangle = \frac{1}{N}\sum_{\alpha=1}^{N} \boldsymbol{S}^H_\alpha \tag{3.2}$$

with

$$\boldsymbol{S}^H = -\mathscr{R}^{ss}_{\boldsymbol{SU}}\cdot(\mathscr{R}^{ss}_{\boldsymbol{FU}})^{-1}\cdot\mathscr{R}^{sw}_{\boldsymbol{FU}}\cdot(\boldsymbol{U}^w - \langle \boldsymbol{u}\rangle) + \mathscr{R}^{sw}_{\boldsymbol{SU}}\cdot(\boldsymbol{U}^w - \langle \boldsymbol{u}\rangle). \tag{3.3}$$

The contribution to the stress by the interparticle force is

$$\langle \boldsymbol{S}^P\rangle = \frac{1}{N}\sum_{\alpha=2}^{N}\sum_{\beta<\alpha} \boldsymbol{r}^{\alpha\beta}\boldsymbol{F}^{\alpha\beta} + \mathscr{R}^{ss}_{\boldsymbol{SU}}\cdot(\mathscr{R}^{ss}_{\boldsymbol{FU}})^{-1}\cdot\boldsymbol{F}^P, \tag{3.4}$$

the first term being the purely configurational non-hydrodynamic contribution alluded to in § 2.2, and the second term the hydrodynamic contribution. The summation above is over all particles within the averaging volume. We have defined the stress in the tensile sense, and therefore a positive σ_{yy} (or σ_{xx}) implies tension. The net stress σ_{yy} is simply the normal force F_y on the walls, given by (2.6), divided by area of the wall in the master cell $2L$ (refer to figure 1). Since F_y and S^H_{yy} are computed independently in our simulations, and S^P_{yy} is readily determined for each particle configuration, the isotropic far-field stress Π^H_{ff} can be determined from (3.1). The total particle pressure is then

$$\Pi = \Pi^H_{ff} - \frac{1}{3}\frac{N}{V}\,\mathrm{Tr}\left(\langle \boldsymbol{S}^H\rangle + \langle \boldsymbol{S}^P\rangle\right), \tag{3.5}$$

and the normal stress in the x-direction is

$$\sigma_{xx} = -\Pi^H_{ff} + \frac{N}{V}\left\{\langle S^H_{xx}\rangle + \langle S^P_{xx}\rangle\right\}. \tag{3.6}$$

A detail to bear in mind is that the force on the walls, $\boldsymbol{F}^w$, given by (2.6), includes the contribution due to shear of the layer of pure liquid, which has to be subtracted to

https://doi.org/10.1017/S0022112000008375 Published online by Cambridge University Press

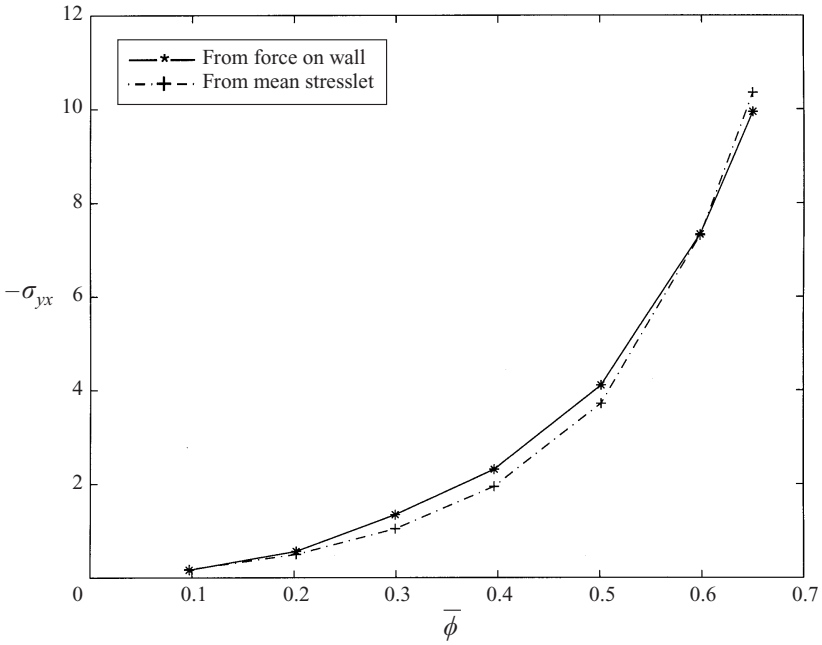


FIGURE 6. Comparison of the shear stress measured on the wall with that derived from the stresslet on the suspended particles. The Couette gap H is 30, and the parameters for the repulsive inter-particle force are as in figure 3.

determine the shear stress within the suspension. This is done by simply subtracting $\eta 2U_0/H$ from the stress determined from (2.6). All the results reported in this section are obtained with the strength and range of the repulsive force fixed, $F_0 = 10^{-4}$, $\tau = 100$. We consider the effect of varying these parameters on the rheology in § 3.2.

Figure 6 displays the dimensionless shear stress (or the relative viscosity of the suspension) as a function of the mean area fraction of particles for a Couette gap of 30, determined from the force on the walls (solid line) and from the mean stresslet $\langle S_{xy} \rangle$ on the suspended particles (dot-dashed line). It is apparent that the agreement between the two measurements is very good. Figure 7 shows that increasing the Couette gap H has very little effect on the shear stress, implying that the flow is that of uniform shear even for the smallest Couette gap we have considered. The shear stress increases rapidly as the concentration approaches that of maximum random packing (which is $\bar{\phi} \approx 0.83$ for a monolayer of spheres), as expected.

We now turn to the normal stresses determined from our simulations; figure 8 shows the dimensionless σ_{yy} as a function of the particle concentration, determined from the normal force on the walls (as mentioned earlier, $-\sigma_{yy}$ is the compressive normal stress). It is zero and has zero slope at $\bar{\phi} = 0$, in agreement with the predicted ϕ^2 variation (Brady & Morris 1997) for dilute suspensions. It is also apparent that σ_{yy} rises rapidly with $\bar{\phi}$, with the suggestion of a divergence as maximum random packing is approached. This suggests that the normal stress in the gradient direction can be measured experimentally at moderate to high concentrations. The scatter in the data and the variation with H are higher than for the shear stress, primarily a result of the sensitivity of the normal stress to the microstructure. The scatter can be minimized by averaging over many configurations, but the low mobility of particles at high concentrations reduces the scope for averaging over many configurations

https://doi.org/10.1017/S0022112000008375 Published online by Cambridge University Press

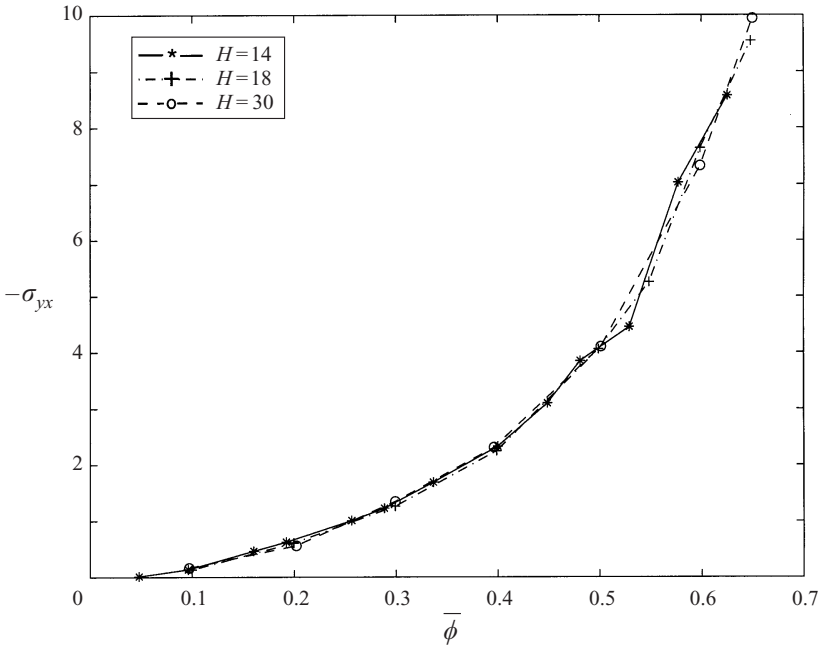


FIGURE 7. The shear stress σ_{yx} at the wall as a function of the mean area fraction for Couette gaps of 14, 18 and 30. The parameters for the repulsive inter-particle force are as in figure 3.

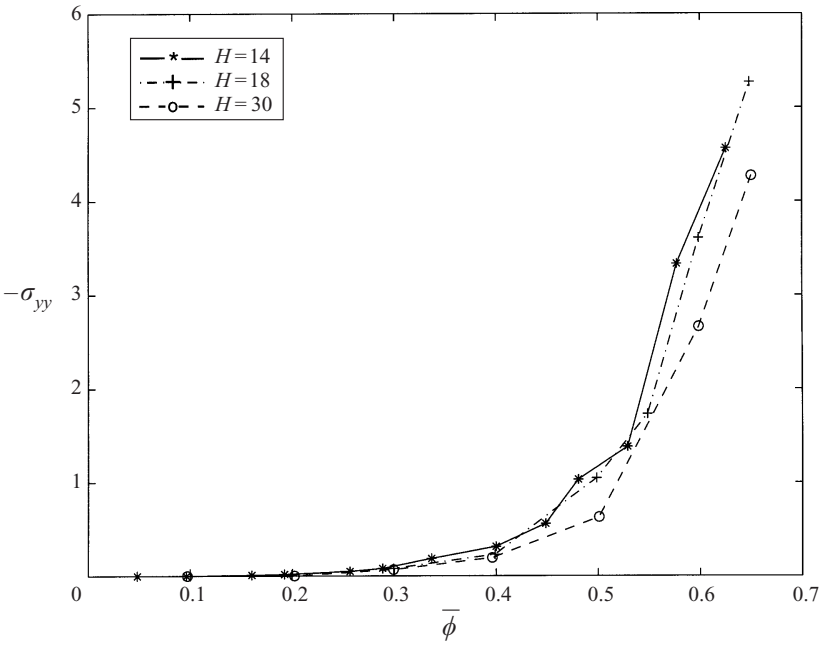


FIGURE 8. The normal stress σ_{yy}, measured on the wall, as a function of the mean area fraction of suspended particles. The parameters for the repulsive inter-particle force are as in figure 3.

https://doi.org/10.1017/S0022112000008375 Published online by Cambridge University Press

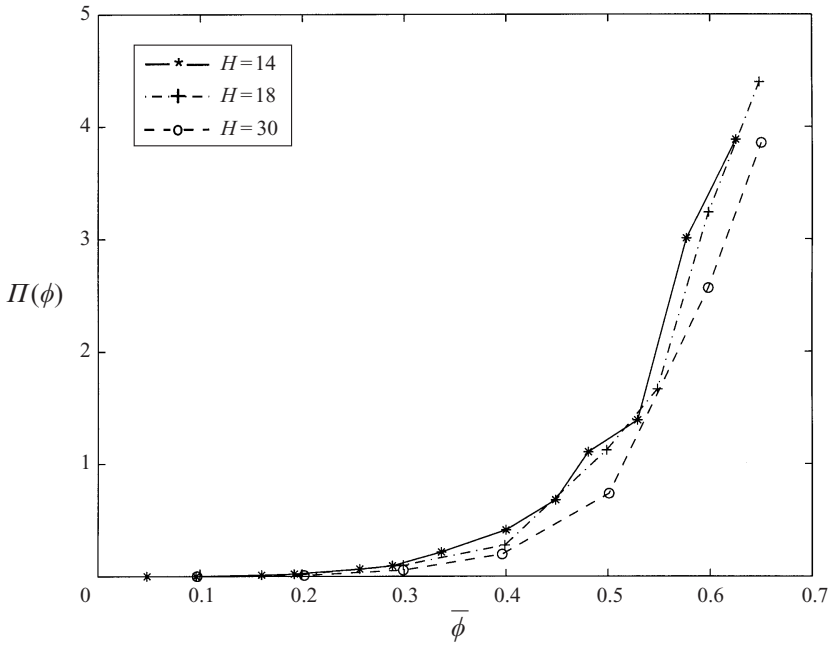


FIGURE 9. The isotropic part of the particle stress, $\Pi(\phi)$. The parameters for the repulsive inter-particle force are as in figure 3.

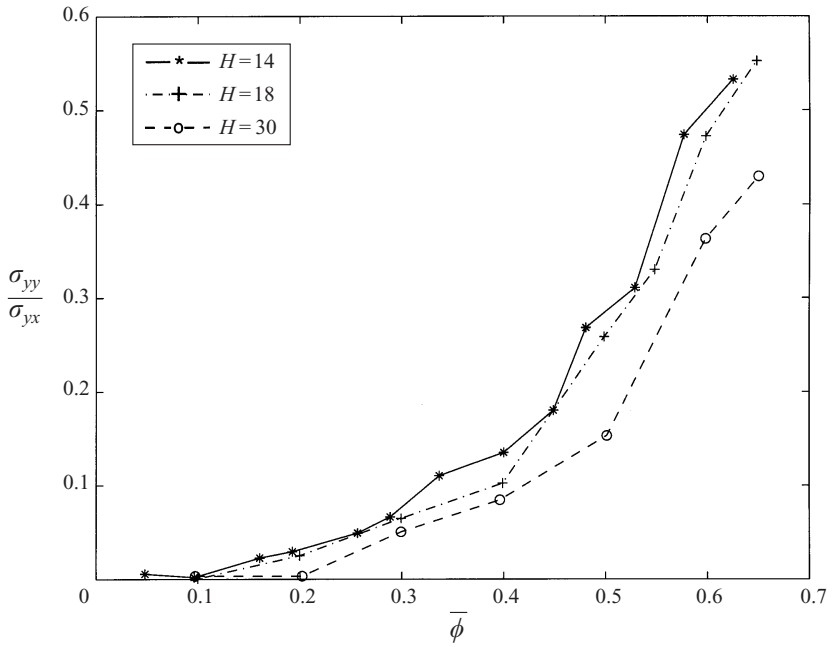


FIGURE 10. The ratio of normal to shear stresses as a function of the mean area fraction. The parameters for the repulsive inter-particle force are as in figure 3.

https://doi.org/10.1017/S0022112000008375 Published online by Cambridge University Press

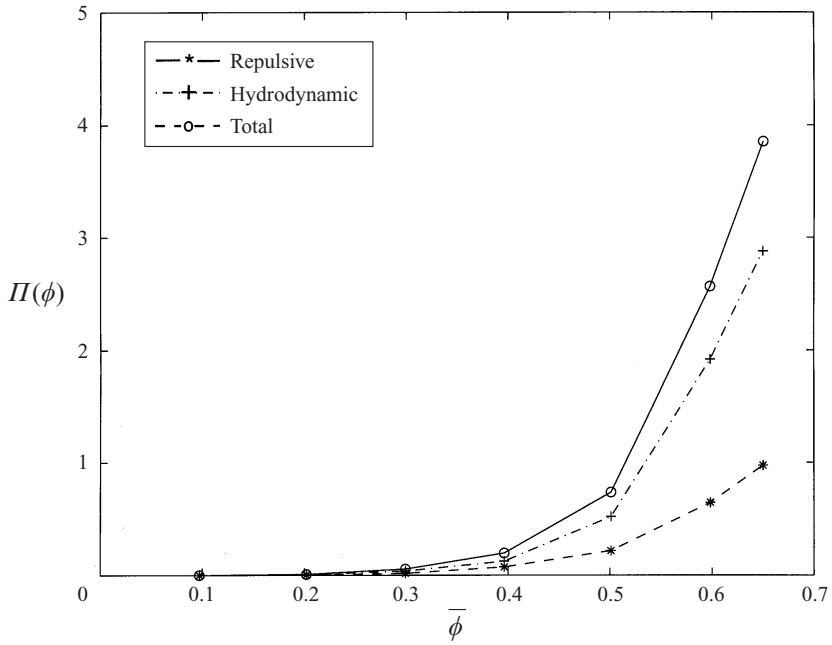


FIGURE 11. The hydrodynamic and repulsive-force contributions to the particle pressure. The Couette gap is 30, and the inter-particle repulsive force parameters are as in figure 3.

in a single simulation. We were constrained from obtaining an ensemble average over many initial configurations by the large computation time required for each simulation. The variation with H is probably a result of the structure being distorted by the walls over a significant fraction of the shearing layer when the gap is small.

The isotropic part of the particle stress is shown in figure 9 as a function of the concentration; the trends are similar to those in figure 8. Though very small at low concentrations, the magnitude of the pressure approaches that of the shear stress with increasing concentration. Figure 10 clearly shows the ratio σ_{yy}/σ_{yx} increasing with the particle concentration. This is an interesting and useful result, because Nott & Brady (1994) have demonstrated that this ratio must be a monotonic increasing function of the particle concentration for the stability of homogeneous shear to perturbations in the particle concentration. The contributions of the hydrodynamic and inter-particle stresses to the particle pressure are given in figure 11. The contribution from the repulsive force is much smaller than the hydrodynamic contribution, but it is nevertheless significant. As discussed earlier in § 2.2, the division of the total pressure into the two components is only nominal, as it does not reflect the respective contributions to the microstructure; this is further explored in § 3.2.

Finally, the first normal stress difference, $N_1 \equiv \sigma_{xx} - \sigma_{yy}$, is shown in figure 12 as a function of the particle concentration. It is always negative, in agreement with the simulation data of Phung *et al.* (1996), and its magnitude rises rapidly with $\bar{\phi}$. At small concentrations, the contribution to N_1 from the repulsive force is very small; its magnitude is significant at large concentrations, but it is of opposite sign to the hydrodynamic contribution. Since our simulations are for monolayers, we are unable to determine the second normal stress difference $N_2 \equiv \sigma_{yy} - \sigma_{zz}$.

https://doi.org/10.1017/S0022112000008375 Published online by Cambridge University Press

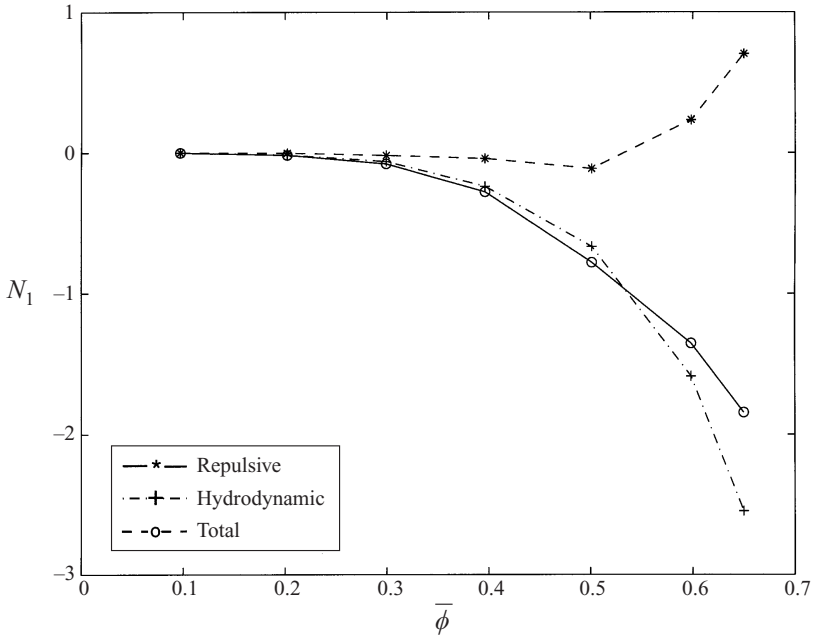


FIGURE 12. The net first normal stress difference, N_1, and its hydrodynamic and repulsive-force components for $H = 30$ as a function of the mean particle area fraction. The inter-particle repulsive force parameters are as in figure 3. The repulsive-force component is always much smaller than the hydrodynamic contribution, and is of opposite sign at large concentrations.

$F_o\tau$	τ	$-\sigma_{yx}$	$-\sigma^H_{yx}$	$-\sigma^P_{yx}$	$-\sigma_{yy}$	$-\sigma^H_{yy}$	$-\sigma^P_{yy}$
0.01	10	2.1175	2.1634	−0.1274	0.2514	0.0912	0.1602
0.01	100	2.2706	2.3308	−0.1051	0.3044	0.2379	0.0665
0.01	1000	2.3269	2.4054	−0.0759	0.2293	0.1957	0.0336
0.01	10000	2.3922	2.4567	−0.0503	0.2182	0.2082	0.0100
0.01	100	2.2706	2.3308	−0.1051	0.3044	0.2379	0.0665
0.10	100	2.1517	2.1793	−0.1252	0.2873	0.1747	0.1126
1.00	100	2.0818	2.0600	−0.1063	0.2858	0.1049	0.1809
10.0	100	2.0174	1.9469	−0.0691	0.2595	0.0380	0.2215

TABLE 1. Effect of the inter-particle repulsive interaction on the rheology. The mean particle area fraction is 0.4 and the Couette gap is 18. The superscripts H and P refer to the contributions to the stress from the hydrodynamic and the repulsive interactions, respectively. Column 3 gives the net shear stress and column 6 gives the net normal stress.

3.2. *Effect of the repulsive force on the rheology*

The inter-particle repulsive interaction contributes to the bulk stress in two ways: a direct contribution, given by (3.4), and an indirect contribution that arises from its effect on the microstructure. We now consider the net effect of the repulsive force on the rheology by computing the stress for a range of the parameters F_0 and τ which specify the repulsive interaction (see equation (2.9)).

For a Couette gap of 18 and mean particle area fraction of 0.40, simulations were performed for F_0 and τ varying over three orders of magnitude, the results of which are tabulated in table 1. The hydrodynamic and inter-particle force contributions to

https://doi.org/10.1017/S0022112000008375 Published online by Cambridge University Press

the shear and normal stresses are given separately. A feature that is immediately apparent is that the variation of the net shear and normal stresses over such a large range of these parameters is quite modest. The hydrodynamic contributions show a decreasing trend with increasing $F_0\tau$ (it is this product that determines the repulsive force, see equation (2.9)). The most notable point here is that the hydrodynamic contribution to the normal stress increases as the strength of the repulsive force decreases. From the data in the first four rows of table 1, we observe the rough trend of a slight rise in the hydrodynamic normal stress as the range of the repulsive force decreases. These observations contrast with the predictions of Brady & Morris (1997) that the normal stresses vanish as $(b/a-1)^{0.22}$ as $b/a \to 1$, where b is the effective hard-sphere radius of the particles. We attempted a simulation with no inter-particle repulsion, but encountered repeated particle overlap even at a time increment of 10^{-3}; we could not attempt even lower increments as the computation time was excessive. Therefore, we are unable to comment on whether normal stresses are present when there is no repulsive interaction between particles at all.

While our observation of a rise in the magnitude of the normal stresses as the strength or range of the repulsion is reduced is in conflict with the prediction of Brady & Morris, a suggestion in their paper may explain the trend of our data. Brady & Morris argue that in the absence of Brownian motion, a weak repulsion between particles will yield an anisotropy in the pair distribution in a boundary layer whose thickness is determined by the ratio of repulsive to shear forces, having much the same consequence on rheology as when there is weak Brownian motion. In other words, the limit of no repulsion is singular, as is the limit of $Pe \to \infty$, and there will be an $O(1)$ contribution to the rheology from the boundary layer whose thickness scales as the inverse of the range of the repulsive force. Our normal stress data appear to follow such a trend, and so do our data on the pair distribution (see below).

3.3. *Microstructure*

For non-Brownian suspensions of rigid spheres in a Newtonian liquid in the creeping flow regime, non-Newtonian rheology can only arise from anisotropy in the microstructure. The anisotropy in the pair distribution function of particles has been determined in experiments by Parsi & Gadala-Maria (1987), in simulations by Bossis & Brady (1984) and Phung *et al.* (1996), and from analysis by Brady & Morris (1997). Here, we report the pair-distribution function inferred from our simulations. Our intention is to explore and emphasize the link between anisotropy in the microstructure and normal stresses that was made by Brady & Morris (1997).

Owing to the presence of the impenetrable walls, the pair-distribution function is a function not just of the relative coordinates r and θ, but also of the absolute coordinate y, i.e. $g = g(r, \theta, y)$. Here θ is measured counter-clockwise from the positive x-axis (see figure 1). The pair distribution was determined in the usual manner, by choosing a sample particle and counting the number of its neighbours centred within each discretized area in the (r, θ)-plane; the computed pair probability is then assigned to the centre of the discretized area. The area discretization was accomplished by marking concentric circles centred at the sample particle, and lines radiating from it. The concentric circles were marked with a radius increment of 10^{-5} for $2 < r < 2.001$, 10^{-3} for $2.001 < r < 2.1$, and 10^{-1} thereafter until $r = 4.5$; this grid refinement was necessary to resolve the buildup of particles near contact. The radial lines were marked to subtend angles in integral multiples of 18° with the x-axis. The measurements were averaged over all particles within a specified range of y, and over a long period of time.

https://doi.org/10.1017/S0022112000008375 Published online by Cambridge University Press

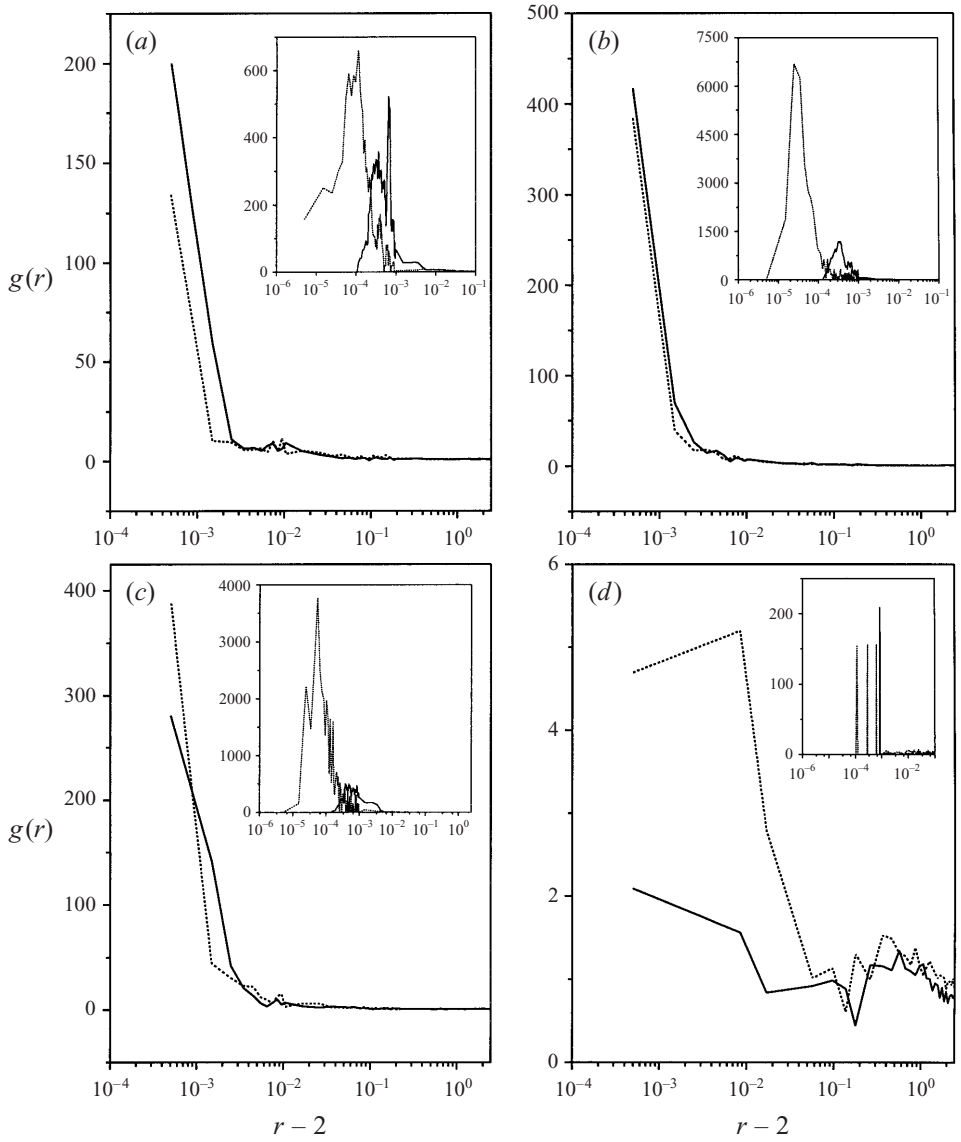


FIGURE 13. The pair-distribution function $g(r,\theta)$ at the symmetry axis of the Couette gap. (*a*) $\theta = 9°$, (*b*) $\theta = 45°$, (*c*) $\theta = 81°$, (*d*) $\theta = 153°$: the angle θ is measured counter-clockwise from the positive x-axis, so $0° < \theta < 90°$ corresponds to the upstream side (the compression quadrant) of the reference sphere and $90° < \theta < 180°$ to the downstream side (extension quadrant). Parameters are $\bar{\phi} = 0.4$, $H = 18$, and $F_0\tau = 10^{-2}$ with $\tau = 100$ (solid line) and $\tau = 1000$ (dotted line). Note the substantial buildup very near contact in the compression quadrant, shown in the inset of each panel.

Figure 13 shows the radial dependence of the pair distribution for a few angular positions in the compression quadrant ($0° < \theta < 90°$) and one position in the extension quadrant ($90° < \theta < 180°$); it decays rapidly from its contact value to unity as r increases. There is an enormous buildup of the pair distribution very near contact in the compression quadrant. Comparison of the solid and dashed lines gives an indication of the effect of the range of the repulsive force (the strength $F_0\tau$ is

https://doi.org/10.1017/S0022112000008375 Published online by Cambridge University Press

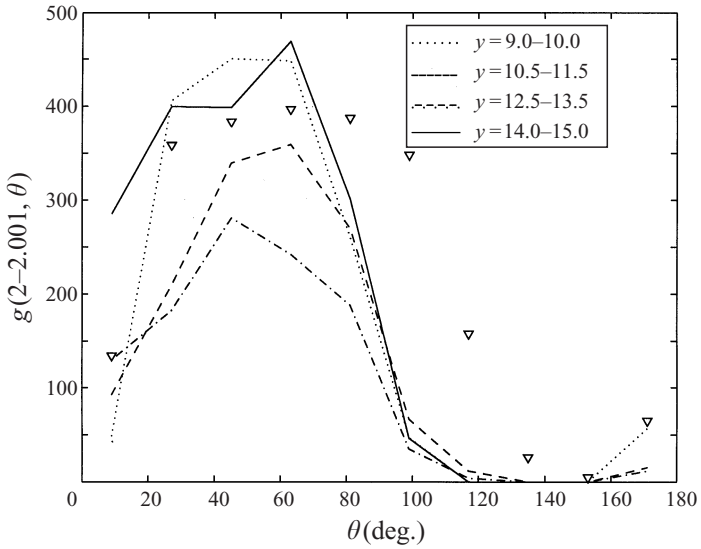


FIGURE 14. The angular dependence of the pair-distribution function near contact for various positions y in the shearing layer. The strong buildup close to contact is not resolved in this plot; shown is $g(r, \theta, y)$ averaged over the range $2 < r < 2.001$. Parameters as in figure 13, except that the symbols are for $F_0 = 10^{-5}$, $\tau = 1000$ in the range $y = 9\text{–}10$.

equal to 0.01 in both cases). The buildup in the compression quadrant is much higher and nearer contact for $\tau = 1000$; they differ by roughly an order of magnitude at the compression axis ($\theta = 45°$).

Figure 14 shows the angular variation of the pair distribution near contact for various ranges of y. This figure does not resolve the large buildup very near contact that is evident in figure 13, as $g(r, \theta)$ is calculated in a shell of thickness 10^{-3} around contact, which yields an average value across the boundary layer. Considerable enhancement of the pair probability in the compression quadrant is evident, as in the unbounded shear simulations of Bossis & Brady (1984). That the magnitude of the distribution for $\tau = 100$ and 1000 are very similar indicates that the net buildup within the boundary layer for the two cases is roughly the same. This figure suggests that τ has some effect on the nature of asymmetry as well, as the enhancement in the pair distribution persists into a good part of the extension quadrant for $\tau = 1000$.

Our simulations do not indicate any substantial dependence of the pair distribution on the Couette gap H; further, the qualitative trends shown in figures 13 and 14 are also insensitive to variation in $\bar{\phi}$, though the extent of enhancement in the compression quadrant increases with $\bar{\phi}$.

It is thus clear that there is significant enhancement of the pair probability in the compression quadrant. It is this fore–aft asymmetry in the microstructure that gives rise to the hydrodynamic contribution to the normal stress differences and the isotropic pressure. While Brady & Morris (1997) have attempted to determine the contribution to the rheology arising from pair interactions, there is surely a significant contribution from many-body hydrodynamic interactions; we address this issue in the concluding section. We have not computed the microstructure for a large enough range of τ to comment definitively on the prediction of Brady & Morris (1997) that the enhancement in the pair distribution at contact scales inversely with the range of the repulsive force, but our limited data appear to follow this prediction. Moreover,

https://doi.org/10.1017/S0022112000008375 Published online by Cambridge University Press

the integral

$$\int_{0<\theta<90} g(r,\theta)\mathrm{d}r\,\mathrm{d}\theta,$$

which determines the contribution to the stress from the boundary layer, remains insensitive to the range of the repulsive force, also in agreement with the prediction of Brady & Morris.

4. Summary and conclusion

We have determined the rheology of a non-Brownian suspension via Stokesian Dynamics simulations. Our study differs from earlier simulation studies in that we have considered bounded shear, and determined the stresses from the forces on the walls, just as one would in an experiment. We have determined the shear and normal stresses as a function of the mean particle concentration $\bar{\phi}$, the Couette gap H, and the strength and range of the imposed inter-particle repulsive force.

This study unambiguously demonstrates the existence of an isotropic particle pressure as well as normal stress differences in sheared suspensions. The normal stresses are small (in comparison with the shear stress) at low particle concentration $\bar{\phi}$, but rise rapidly with $\bar{\phi}$ (see figures 8 and 10). They are, however, relatively insensitive to the Couette gap H. The particle pressure and the first normal stress difference follow the same trend. The latter is negative (when the stress is defined in the tensile sense), in agreement with the results of Phung *et al.* (1996) for large Péclet number. The ratio of the normal to shear stresses, σ_{yy}/σ_{yx}, is also a monotonic increasing function of $\bar{\phi}$, substantiating the analysis of Nott & Brady (1994) that showed this to be a condition for stability of a homogeneous suspension in uniform shear.

Normal stress differences from simulations have been reported earlier by Brady & Bossis (1985) for non-Brownian suspensions and by Phung *et al.* (1996) for Brownian suspensions, both of whom considered unbounded plane shear. They were unable to determine the particle pressure, as the isotropic part of the particle stresslet was taken to be zero while computing the far-field part of the hydrodynamic interactions. Using the analytical expressions of Jeffrey *et al.* (1993) for the hydrodynamic functions that determine the isotropic particle stresslet, Yurkovetsky (1997) has recently determined the particle pressure for unbounded shear. As stated above, we have followed the more direct approach of determining the particle pressure from the normal force on the bounding walls; our study therefore complements that of Yurkovetsky.

The issue of normal stresses in suspensions merits serious study for two important reasons. The first is that it is an indication of non-Newtonian behaviour of a mixture that has for long been thought of as Newtonian – it does not exhibit the more common non-Newtonian features of shear thinning or thickening. Secondly, a case has been made for the close linkage of the normal stresses to shear-induced migration of particles in inhomogeneous shear fields by Nott & Brady (1994) and Morris & Boulay (1999). The discussion in the introductory section points out the lack of direct experimental measurements of the normal stresses on well-characterized systems in the viscous regime, and motivates the necessity for pursuit in this direction.

The pair-distribution function determined from our simulations clearly shows anisotropy in the microstructure, which is the cause of normal stresses. Brady & Morris (1997) argued that a balance between a small amount of Brownian diffusion (i.e. $Pe \to \infty$) and advection determines the pair probability; the result is an enhance-

https://doi.org/10.1017/S0022112000008375 Published online by Cambridge University Press

ment in the pair probability of $O(Pe)$ in a boundary layer of thickness $O(Pe^{-1})$ in the compression quadrant. Our simulations are in the precise limit of $Pe = \infty$, and therefore cannot test this prediction. However, we do observe a large buildup of particles near contact in the compression quadrant. The normal stresses we have determined show a general trend of increasing as the strength and range of the inter-particle repulsive force is decreased (see table 1). This contrasts with the prediction of Brady & Morris that the normal stresses scale as $(b/a - 1)^{0.22}$ as $b/a \to 1$, where b is the hard-sphere repulsion radius and a the radius of the spheres. However, their argument that in the absence of Brownian motion, the balance between a weak repulsion and advection will still result in an anisotropic microstructure in a thin boundary layer, and therefore normal stresses, appears to have merit. Our observations of the stress being insensitive to variation of the strength and range of the repulsive force over a wide range, and the pair distribution near contact increasing as the range is decreased lend support to their argument.

In a recent paper, Haan & Steif (1993) have also determined the 'particle-phase pressure' by simulating shear flow of a planar suspension cylinders. While the objectives of their study and ours are very similar, their simulation technique is very different: they solve the Navier–Stokes equations in the entire fluid domain, while the Stokesian Dynamics method enables us to solve for the particle velocities alone without computing the detailed motion of the fluid. Haan & Steif argue that surface roughness is key to the development of particle-phase pressure and the anisotropy in the microstructure, but the manner in which they have numerically accounted for roughness is in essence similar to imposing a repulsive force between particles. However, the range of the repulsive force in our simulations is much smaller than the 'contact threshold' of Haan & Steif, and is therefore more appropriate for comparison with the predictions of Brady & Morris. The results on microstructure that we present are more detailed and clearly show the singular nature of the enhancement of the pair probability in the compression quadrants that Brady & Morris predicted. Lastly, and perhaps most importantly, Haan & Steif calculate the dispersive pressure as the difference between the isotropic part of the stress in the particle and the fluid phases. However, the accepted definition of the particle-induced stress is the difference between the stress in a suspension and that in a pure fluid undergoing the same macroscopic deformation (see, for example, Batchelor 1970). It is not clear what the physical relevance of the differential phase pressure reported by Haan & Steif is, but it is certainly not what one can measure in an experiment. Indeed, the normal stress on the walls that we measure in our simulations results entirely from the stress in the fluid adjacent to the wall.

The model of Brady & Morris determines the contribution to the rheology from pair interactions, arguing that the pair distribution is determined from an interplay of a weak Brownian motion, repulsive inter-particle force, and hydrodynamic pair interaction. They show that this produces a large enhancement of the pair distribution in a thin boundary layer in the compression quadrant, and that this enhancement leads to a finite contribution to the normal stresses. Our data in figures 13 and 14 clearly corroborate the singular nature of the enhancement that Brady & Morris predict. However, there is also the distinct possibility of a contribution to the rheology from asymmetry in the microstructure outside the boundary layer, and not necessarily arising from pair interactions alone. In this context, we speculate that the anisotropy in the hydrodynamic (non-Brownian) diffusion that many studies have reported can perhaps cause an asymmetry in the microstructure, and therefore normal stresses. This speculation may be explored using the recent phenomenological model of Levine *et al.*

https://doi.org/10.1017/S0022112000008375 Published online by Cambridge University Press

(1998), who argue that the appropriate coarse-grained equation for the concentration fluctuation in a sedimenting suspension is a generalized Langevin equation characterized by a diffusivity and a random current. Using this approach they predict the existence of 'screened' and 'unscreened' phases in sedimenting suspensions, referring to the velocity variance of particles being independent of system size (as observed in experiments) and varying with the system size, respectively. Their result hinges on the premise that the diffusivity and the random current are anisotropic, and are not related by a fluctuation–dissipation theorem. It would be interesting to explore this model in the context of rheology, as it would complement the effort of Brady & Morris.

There is an important consequence of the presence of normal stresses that has not been explored by experiment yet, and that is its effect on traction-free surfaces. Consider, as an example, shear in a cylindrical Couette device, with the suspension filled to a certain height in the gap. Within the suspension, normal stresses are generated due to shear, but the normal traction (in excess of the atmospheric pressure) on the free surface must be zero. This could result in the concentration of particles varying, as a function of distance from the surface, in such a way that the normal stress decays to zero as the free surface is approached. Alternatively, the pressure in the fluid phase must reduce to compensate the (compressive) normal stress due to the particles. A proper study of suspension flows with free surfaces is necessary to throw light on this interesting problem.

The idea of conducting Stokesian Dynamics simulations of bounded shear was conceived many years ago during discussions with John F. Brady and Jeffrey F. Morris – we wish to thank them for their suggestions. This project was funded in part by the Department of Science and Technology under project number III 5(90)/95-ET. PRN also wishes to acknowledge the facilities provided by the California Institute of Technology, where he was on sabbatical when this paper was completed.

REFERENCES

Bagnold, R. A. 1954 Experiments on a gravity-free dispersion of large solid spheres in a Newtonian fluid under shear. *Proc. R. Soc. Lond.* A **225**, 49.

Batchelor, G. K. 1970 The stress system in a suspension of force-free particles. *J. Fluid Mech.* **41**, 545.

Bossis, G. & Brady, J. F. 1984 Dynamic simulation of sheared suspensions. I. General method. *J. Chem. Phys.* **10**, 5141.

Brady, J. F. & Bossis, G. 1985 The rheology of concentrated suspensions of spheres in simple shear flow by numerical simulation. *J. Fluid Mech.* **155**, 105.

Brady, J. F. & Bossis, G. 1988 Stokesian Dynamics. *Ann. Rev. Fluid Mech.* **20**, 111.

Brady, J. F., Phillips, R. J., Lester, J. C. & Bossis, G. 1988 Dynamic simulation of hydrodynamically interacting suspensions. *J. Fluid Mech.* **195**, 257.

Brady, J. F. & Morris, J. F. 1997 Microstructure of strongly sheared suspensions and its impact on rheology and diffusion. *J. Fluid Mech.* **348**, 103.

Brenner, H. 1961 The slow motion of a sphere through a viscous fluid towards a plane surface. *Chem. Engng Sci.* **16**, 242.

Cox, R. G. & Brenner, H. 1967 The slow motion of a sphere through a viscous fluid towards a plane surface – II. Small gap widths, including inertial effects. *Chem. Engng Sci.* **22**, 1753.

Dean, W. R. & O'Neill, M. E. 1963 A slow motion of viscous liquid caused by the rotation of a solid sphere. *Mathematika* **10**, 13.

Dratler, D. I. & Schowalter, W. R. 1996 Dynamic simulation of suspensions of non-Brownian hard spheres. *J. Fluid Mech.* **325**, 53.

https://doi.org/10.1017/S0022112000008375 Published online by Cambridge University Press

Durlofsky, L. & Brady, J. F. 1989 Dynamic simulation of bounded suspensions of hydrodynamically interacting particles. *J. Fluid Mech.* **200**, 39.

Durlofsky, L., Brady, J. F. & Bossis, G. 1987 Dynamic simulation of hydrodynamically interacting particles. *J. Fluid Mech.* **180**, 21.

Gadala-Maria, F. A. 1979 The rheology of concentrated suspension. PhD thesis, Stanford University.

Ganatos, P., Weinbaum, S. & Pfeffer, R. 1982 Gravitational and zero-drag motion of a sphere of arbitrary size in an inclined channel at low Reynolds number. *J. Fluid Mech.* **124**, 27.

Goldman, A. J., Cox, R. G. & Brenner, H. 1967 Slow viscous motion of a sphere parallel to a plane wall – I. Motion through a quiescent fluid. *Chem. Engng Sci.* **22**, 637.

Haan, J. J. & Steif, P. S. 1998 Particle-phase pressure in a slow shearing flow based on the numerical simulation of a planar suspension of rough contacting cylinders *J. Rheol.* **42** (4), 891.

Jeffrey, D. J., Morris, J. F. & Brady, J. F. 1993 The pressure moments for two spheres in a low-Reynolds-number flow. *Phys. Fluids* A **5**, 2317.

Jenkins, J. T. & McTigue, D. F. 1990 Transport processes in concentrated suspensions: the role of particle fluctuations. In *Two Phase Flow and Waves* (ed. D. D. Joseph & D. G. Schaeffer). Springer.

Leighton, D. & Acrivos, A. 1987 The shear-induced migration of particles in concentrated suspensions. *J. Fluid Mech.* **181**, 415.

Levine, A., Ramaswamy, S., Frey, E. & Bruinsma, R. 1998 Screened and unscreened phases in sedimenting suspensions. *Phys. Rev. Lett.* **81**, 5944.

Maude, A. D. 1961 End effects in a falling sphere viscometer. *Brit. J. Appl. Phys.* **12**, 293.

Morris, J. F. & Bouley, F. 1999 Curvilinear flows of noncolloidal suspensions: the role of normal stresses. *J. Rheol.* **43**, 1213.

Nott, P. R. & Brady, J. F. 1994 Pressure-driven flow of suspensions: simulation and theory. *J. Fluid Mech.* **275**, 157.

O'Neill, M. E. 1964 A slow motion of viscous liquid caused by a slowly moving solid sphere. *Mathematika* **11**, 67.

Parsi, F. & Gadala-Maria, F. A. 1987 Fore-and-aft asymmetry in a concentrated suspension of solid spheres. *J. Rheol.* **31**, 725.

Phung, T. N., Brady, J. F. & Bossis, G. 1996 Stokesian Dynamics simulation of Brownian suspensions. *J. Fluid Mech.* **313**, 181.

Prasad, D. & Kytomaa, H. K. 1995 Particle stress and viscous compaction during shear of dense suspensions. *Intl J. Multiphase Flow* **21**, 775.

Yurkovetsky, Y. 1997 I. Statistical mechanics of bubbly liquids. II. Behavior of sheared suspensions of non-Brownian particles. PhD thesis, California Institute of Technology.

https://doi.org/10.1017/S0022112000008375 Published online by Cambridge University Press